The Astrophysical Journal, 975:196 (12pp), 2024 November 10 https://doi.org/10.3847/1538-4357/ad79ec

TEMPLATES: Direct Abundance Constraints for Two Lensed Lyman-break Galaxies

Brian Welch[1,2,3], Grace M. Olivier[4], Taylor A. Hutchison[2], Jane R. Rigby[5], Danielle A. Berg[6], Manuel Aravena[7], Matthew B. Bayliss[8], Jack E. Birkin[4], Scott C. Chapman[9,10,11], Håkon Dahle[12], Michael D. Gladders[13], Gourav Khullar[14], Keunho J. Kim[15], Guillaume Mahler[16], Matthew A. Malkan[17], Desika Narayanan[18,19], Kedar A. Phadke[20,21], Keren Sharon[22], J. D. T. Smith[23], Manuel Solimano[7], Justin S. Spilker[4], Joaquin D. Vieira[20,21,24], and David Vizgan[20]

[1] Department of Astronomy, University of Maryland, College Park, MD 20742, USA; brian.d.welch@nasa.gov
[2] Observational Cosmology Lab, NASA Goddard Space Flight Center, Greenbelt, MD 20771, USA
[3] Center for Research and Exploration in Space Science and Technology, NASA/GSFC, Greenbelt, MD 20771, USA
[4] Department of Physics and Astronomy and George P. and Cynthia Woods Mitchell Institute for Fundamental Physics and Astronomy, Texas A&M University, 4242 TAMU, College Station, TX 77843-4242, USA
[5] Astrophysics Science Division, Code 660, NASA Goddard Space Flight Center, 8800 Greenbelt Rd., Greenbelt, MD 20771, USA
[6] Department of Astronomy, The University of Texas at Austin, 2515 Speedway, Stop C1400, Austin, TX 78712, USA
[7] Instituto de Estudios Astrofísicos, Facultad de Ingeniería y Ciencias, Universidad Diego Portales, Avenida Ejército Libertador 441, Santiago, Chile
[8] Department of Physics, University of Cincinnati, Cincinnati, OH 45221, USA
[9] Department of Physics and Atmospheric Science, Dalhousie University, Halifax, NS B3H 4R2, Canada
[10] NRC Herzberg Astronomy and Astrophysics, 5071 West Saanich Rd, Victoria, BC V9E 2E7, Canada
[11] Department of Physics and Astronomy, University of British Columbia, Vancouver, BC V6T 1Z1, Canada
[12] Institute of Theoretical Astrophysics, University of Oslo, P.O. Box 1029, Blindern, NO-0315 Oslo, Norway
[13] Kavli Institute for Cosmological Physics, University of Chicago, 5640 South Ellis Avenue, Chicago, IL 60637, USA
[14] Department of Physics and Astronomy, and PITT PACC, University of Pittsburgh, Pittsburgh, PA 15260, USA
[15] IPAC, California Institute of Technology, 1200 E. California Boulevard, Pasadena, CA 91125, USA
[16] STAR Institute, Quartier Agora—Allée du six Août, 19c B-4000 Liège, Belgium
[17] Department of Physics and Astronomy, University of California, Los Angeles, 430 Portola Plaza, Los Angeles, CA 90095, USA
[18] Department of Astronomy, University of Florida, 211 Bryant Space Sciences Center, Gainesville, FL 32611, USA
[19] Cosmic Dawn Center (DAWN), Niels Bohr Institute, University of Copenhagen, Jagtvej 128, København N, Copenhagen DK-2200, Denmark
[20] Department of Astronomy, University of Illinois Urbana-Champaign, 1002 West Green St., Urbana, IL 61801, USA
[21] Center for AstroPhysical Surveys, National Center for Supercomputing Applications, 1205 West Clark Street, Urbana, IL 61801, USA
[22] Department of Astronomy, University of Michigan, 1085 S. University Ave, Ann Arbor, MI 48109, USA
[23] Department of Physics and Astronomy, Ritter Astrophysical Research Center, University of Toledo, Toledo, OH 43606, USA
[24] Department of Physics, University of Illinois Urbana-Champaign, 1110 West Green St., Urbana, IL 61801, USA
Received 2024 January 23; revised 2024 July 22; accepted 2024 August 14; published 2024 November 4

Abstract

Using integrated spectra for two gravitationally lensed galaxies from the JWST TEMPLATES Early Release Science program, we analyze faint auroral lines, which provide direct measurements of the gas-phase chemical abundance. For the brighter galaxy, SGAS1723+34 ($z = 1.3293$), we detect the [O III] λ4363, [S III] λ6312, and [O II] $\lambda\lambda$7320, 7330 auroral emission lines, and set an upper limit for the [N II] λ5755 line. For the second galaxy, SGAS1226+21 ($z = 2.925$), we do not detect any auroral lines, and report upper limits. With these measurements and upper limits, we constrain the electron temperatures in different ionization zones within both of these galaxies. For SGAS1723+34, where auroral lines are detected, we calculate direct oxygen and nitrogen abundances, finding an N/O ratio consistent with observations of nearby ($z \sim 0$) galaxies. These observations highlight the potent combination of JWST and gravitational lensing to measure faint emission lines in individual distant galaxies and to directly study the chemical abundance patterns in those galaxies.

Unified Astronomy Thesaurus concepts: Galaxies (573); Strong gravitational lensing (1643); Chemical abundances (224)

1. Introduction

The chemical abundances of galaxies are set by the nuclear synthesis of elements in stars, and the recycling of that enriched gas through the interstellar medium (ISM). As the enriched gas is recycled, measurements of the relative abundance of various elements can provide insight into the lives and deaths of previous generations of stars. While astronomers often make the simplifying assumption that the atomic abundance patterns of galaxies are fixed, these patterns in fact should evolve as galaxies evolve.

The gold standard method to calculate atomic abundances in warm interstellar gas is the "direct" method, which utilizes auroral emission lines to measure electron temperature and density in the gaseous nebulae (e.g., H. L. Dinerstein 1990). These temperature and density measurements are then used in association with typically much brighter collisionally excited forbidden line emission to calculate the abundances of individual elements relative to hydrogen.

Application of the direct abundance technique is limited by the fact that auroral emission lines are generally faint, at most a few percent the strength of Hβ. In local galaxies and H II regions, auroral line abundance patterns have been well studied despite the intrinsic faintness of these emission lines (e.g., D. A. Berg et al. 2015, 2020; K. V. Croxall et al. 2015, 2016). However at higher redshift, this faintness has made such

studies more challenging, and therefore only a handful of auroral line detections were possible at Cosmic Noon ($z \sim 1$–3) prior to the launch of JWST (L. Christensen et al. 2012; B. L. James et al. 2014; C. Ly et al. 2015, 2016; R. L. Sanders et al. 2020, 2023).

The difficulty in measuring auroral lines at high redshift leads many to use empirically calibrated relationships between the strengths of strong emission lines and gas-phase metallicity. While these relations can be useful for studies of faint and distant galaxies, previous studies have noted discrepancies between the strong-line metallicity measurements and direct abundances (e.g., G. Stasińska 2005; L. J. Kewley & S. L. Ellison 2008; Á. López-Sánchez et al. 2012). Additionally, the strong-line indicators have been primarily calibrated with local galaxies and H II regions. As galaxies evolve, we expect their atomic abundance patterns to change, and thus we expect the empirical calibrations to evolve with redshift. However, the limited number of auroral line detections at Cosmic Noon and beyond have made such in situ recalibrations difficult.

JWST (J. P. Gardner et al. 2023) has far better sensitivity in the infrared than previous ground- and space-based telescopes (J. Rigby et al. 2023a), and the NIRSpec instrument delivers exquisite near-infrared spectra (T. Böker et al. 2023). Indeed, the first JWST science data released in summer 2022 (of the SMACS J0723 Early Release Observations field; K. M. Pontoppidan et al. 2022) emphatically detected the faint auroral [O III] λ4363 line in galaxies out to $z \sim 8$ (K. Z. Arellano-Córdova et al. 2022; D. Schaerer et al. 2022; A. J. Taylor et al. 2022; J. Brinchmann 2023; M. Curti et al. 2023; H. Katz et al. 2023; J. E. Rhoads et al. 2023; J. R. Trump et al. 2023; J. A. A. Trussler et al. 2023). Early Release Science (ERS) data from CEERS have detected the same line out to $z \sim 8.7$ (R. L. Sanders et al. 2024).

Three Cycle 1 programs were approved to study auroral lines at Cosmic Noon (CECILIA, PID 2593, PI: Strom, co-PI: Rudie; AURORA, PID 1914, PI: Shapley, co-PI: Sanders; and PID 1879, PI: Curti). Multiple auroral lines from nitrogen, sulfur, and oxygen have been detected in a stacked sample at $z \sim 2$–3 from CECILIA, enabling more detailed characterizations of chemical abundances (A. L. Strom et al. 2023). Recently, the CECILIA team have also published detections of oxygen and sulfur auroral lines in a single galaxy (N. S. J. Rogers et al. 2024).

In this paper we present JWST NIRSpec spectra of two bright, gravitationally lensed galaxies at Cosmic Noon. The magnifying effect of gravitational lensing has enabled the detection of multiple auroral lines in one of these galaxies, and set upper limits on these lines for the other galaxy.

This paper is organized as follows. Section 2 describes the data and data reduction processes. Section 3 details how we make our measurements. Section 4 discusses our results, and our conclusions are stated in Section 5. We assume a flat Lambda cold dark matter (ΛCDM) cosmology with $H_0 = 70$ km s^{-1} Mpc^{-1} and $\Omega_m = 0.3$.

2. Data

The data used in this study were taken as part of the TEMPLATES Director's Discretionary Early Release Science (DD-ERS) observing program with JWST (PID 1355, PI: Rigby, co-PI: Viera). TEMPLATES obtained imaging with NIRCam and MIRI, and integral field unit (IFU) spectroscopy with NIRSpec and MIRI/MRS, targeting four gravitationally lensed arcs (J. R. Rigby et al. 2023b). Here we focus on the NIRSpec spectroscopy for two of the four TEMPLATES targets: SGAS1723+34 (R.A. = 17:23:36.406, decl. = +34:11:54.69) at $z = 1.3293$ (J. M. Kubo et al. 2010; K. Sharon et al. 2020; J. R. Rigby et al. 2021) and SGAS1226+21 (R.A. = 12:26:51.296, decl. = +21:52:19.97) at $z = 2.925$ (B. P. Koester et al. 2010; E. Wuyts et al. 2012; K. Sharon et al. 2022). These targets are both blue star-forming galaxies with relatively low dust attenuation and subsolar metallicities, making them the best candidates from TEMPLATES to search for faint auroral line features. The two other TEMPLATES targets are dusty star-forming galaxies (C. M. Casey et al. 2014) with near-solar metallicities (J. E. Birkin et al. 2023). Auoral lines were not targeted in these two dusty star-forming galaxies, and we do not expect to see auroral line emission from such galaxies. Visual inspection of their coadded spectra show no evidence of these lines.

SGAS1723+34 was observed in both the G140H and G395H high spectral resolution ($R \sim 3000$) gratings. For this source, G140H covers the rest-frame wavelength range of ~4100 to ~8100 Å. The second grating was selected to cover the Paα emission line, however we do not use those data in this analysis. SGAS1226+21 was observed using the G235H grating. Further details on the observations can be found in J. R. Rigby et al. (2023b).

The initial set of observations for SGAS1723+34 failed because the telescope drifted off target. However, the initial observation in the G140H grating completed successfully prior to this drift. Both grating settings were reobserved after this error was discovered. Thus we have two full observations of SGAS1723+34 in the G140H grating, each with the originally allocated exposure time of 4435 s. We utilize both of these pointings in this analysis in order to maximize the signal-to-noise ratio (SNR) in our final spectra, resulting in a total usable exposure time of 8870 s. The IFU field of view from both pointings is shown in Figure 1.

The G235H observations of SGAS1226+21 were obtained with an exposure time of 4143 s.

The TEMPLATES NIRSpec data reduction is nontrivial. We will provide a brief description here, and refer the interested reader to J. R. Rigby et al. (2023b) for further details. The TEMPLATES team has released a Jupyter Notebook in Zenodo (Rigby et al. 2024) demonstrating how these reductions were performed.[25] Briefly, we utilize the main JWST reduction pipeline (version 1.11.4; H. Bushouse et al. 2023), with several parameters tailored to our specific needs. We include the `expand-large-events` flag in the `Detector1` pipeline to better flag snowballs. We run NSClean (B. J. Rauscher 2024) to remove correlated read noise from the detector images. We utilize the sigma clipping algorithm of T. A. Hutchison et al. (2024) to remove any outliers that are not dealt with by the `Spec3` pipeline's built-in outlier detection step. T. A. Hutchison et al. (2024) demonstrated that this combination performs better than either tool alone.

The NIRSpec data only reach down to rest-frame wavelengths of 4100 Å for SGAS1723+34, and 4200 Å for SGAS1226+21. The [O II] $\lambda\lambda$3727, 3729 lines, which fall outside the NIRSpec coverage, will be useful for determining electron temperatures in the lower ionization region of the galaxy. For SGAS1723+34, this wavelength range was

[25] https://github.com/JWST-Templates/Notebooks

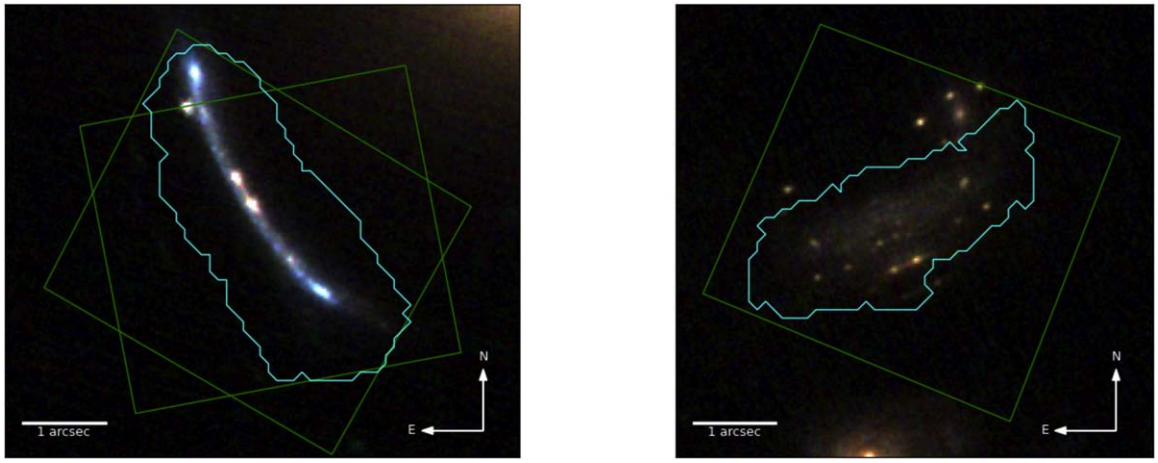

Figure 1. JWST NIRCam color images are shown for SGAS1723+34 (left) and SGAS1226+21 (right). The short-wavelength filters F200W, F150W, and F115W are used for the red, green, and blue channels, respectively. The green boxes in each image represent the NIRSpec IFU field of view. We display the fields of view of the final cubes after dithering, making each slightly larger than the $3'' \times 3''$ single-pointing field of view of the IFU. SGAS1723+34 has two sets of observations in the G140H grating (see Section 2), and we show both in this figure. Cyan contours show the regions used for extraction of the spatially integrated spectra for each target. These regions are based on the SNR of the [O III] λ5007 line, as described in Section 3.1.

covered by Hubble Space Telescope (HST) WFC3 grism data and Keck ESI data, presented in J. R. Rigby et al. (2021). For the present analysis, for any lines blueward of Hγ in SGAS1723+34, we use the observed flux measurements reported in J. R. Rigby et al. (2021), with our own reddening correction applied as described in Section 3.3.1. To account for relative fluxing differences between instruments, we rescale the archival measurements for SGAS1723+34 by Hβ, which is measured by the HST WFC3 grism in J. R. Rigby et al. (2021). This results in the HST fluxes being multiplied by a factor 1.10 ± 0.04. Uncertainties from this rescaling factor are propagated into the resulting line fluxes. To bolster the confidence of using this rescaling, we check the consistency of the Hβ/Hγ line ratio between the HST and JWST data sets. We find that the Hβ/Hγ ratio is consistent within 1σ between the two data sets (2.23 ± 0.06 for JWST, and 2.22 ± 0.2 for HST).

The Keck ESI spectra were scaled to match the HST grism data based on the [O II] $\lambda\lambda$3727, 3729 fluxes. This accounts for potential slit losses from the ESI spectra to first order because the HST grism covers the full width of the source to the sky background limit. Second-order effects (e.g., from spatial variations perpendicular to the arc) could still affect our measurement. Previous studies have not had sufficient SNR to see such variations (e.g., M. K. Florian et al. 2021). We assume that these second-order effects are small and choose to ignore them for the current analysis. Additionally, the aperture from which the HST grism and the JWST/NIRSpec IFU spectra are extracted may be slightly different owing to the change in sensitivity between the two instruments. This small aperture difference is corrected by the rescaling process.

For such blue emission lines in SGAS1226+21, we use fluxes measured from Keck/NIRSPEC reported in E. Wuyts et al. (2012). We apply our own measured reddening correction (described in Section 3.3.1) for consistency. To account for absolute fluxing offsets between the different ground- and space-based observatories, we normalize the literature reported fluxes based on emission lines covered in both data sets. For SGAS1226+21, E. Wuyts et al. (2012) point out that different levels of atmospheric absorption can affect the absolute fluxing of measured emission lines, and they report the atmospheric transmission calculated for each measured line. To account for these differences, we use the [O III] λ4959 line as our normalization, as this line has an atmospheric transmission measurement consistent with [O II] $\lambda\lambda$3727, 3729 in the E. Wuyts et al. (2012) data. This results in a scaling factor of 0.31 ± 0.02. Uncertainties from this rescaling are propagated to the [O II] $\lambda\lambda$3727, 3729 line fluxes. The [O III] λ4959 and [O II] $\lambda\lambda$3727, 3729 lines fall in different filters in this data set, which could potentially impact the relative fluxing of these lines. Additionally, slit losses from the Keck NIRSPEC instrument may impact this calibration, however E. Wuyts et al. (2012) note that the slit covers the entirety of the galaxy, resulting in minimal losses. We do not attempt to correct for further relative fluxing differences between the archival data and the new JWST observations. As a consistency check, we calculate the ratio of the [O III] λ4959/Hβ lines in both data sets, and find that the ratios are consistent within 1σ (7 ± 3 from Keck, and 4.4 ± 0.2 for JWST). However we note that these line ratios fall within a single filter in the Keck observations, while the [O II] $\lambda\lambda$3727, 3729 lines are observed with a separate filter, which may introduce a fluxing offset.

3. Methods

3.1. Extraction of One-dimensional Spectra

We maximize the SNR by collapsing the 3D IFU cube down into a single 1D spectrum for each target. We create these 1D spectra using masks made as part of the sigma clipping process used in data reduction. Each spaxel included in this mask has SNR > 3 for the [O III] λ5007 emission line. Because the SNR threshold is set based on the brightest emission line, we do not employ any additional aperture corrections when creating our final coadded spectrum. Any additional flux scattered outside the aperture area by the instrument PSF will be minimal, particularly in the faint auroral lines on which this analysis is focused. We see no evidence of emission from other bright lines extending beyond this extraction region when visually inspecting the 3D IFU cubes. The final extracted spectra are shown in Figure 2, with zoomed insets showing the auroral lines covered in each spectrum.

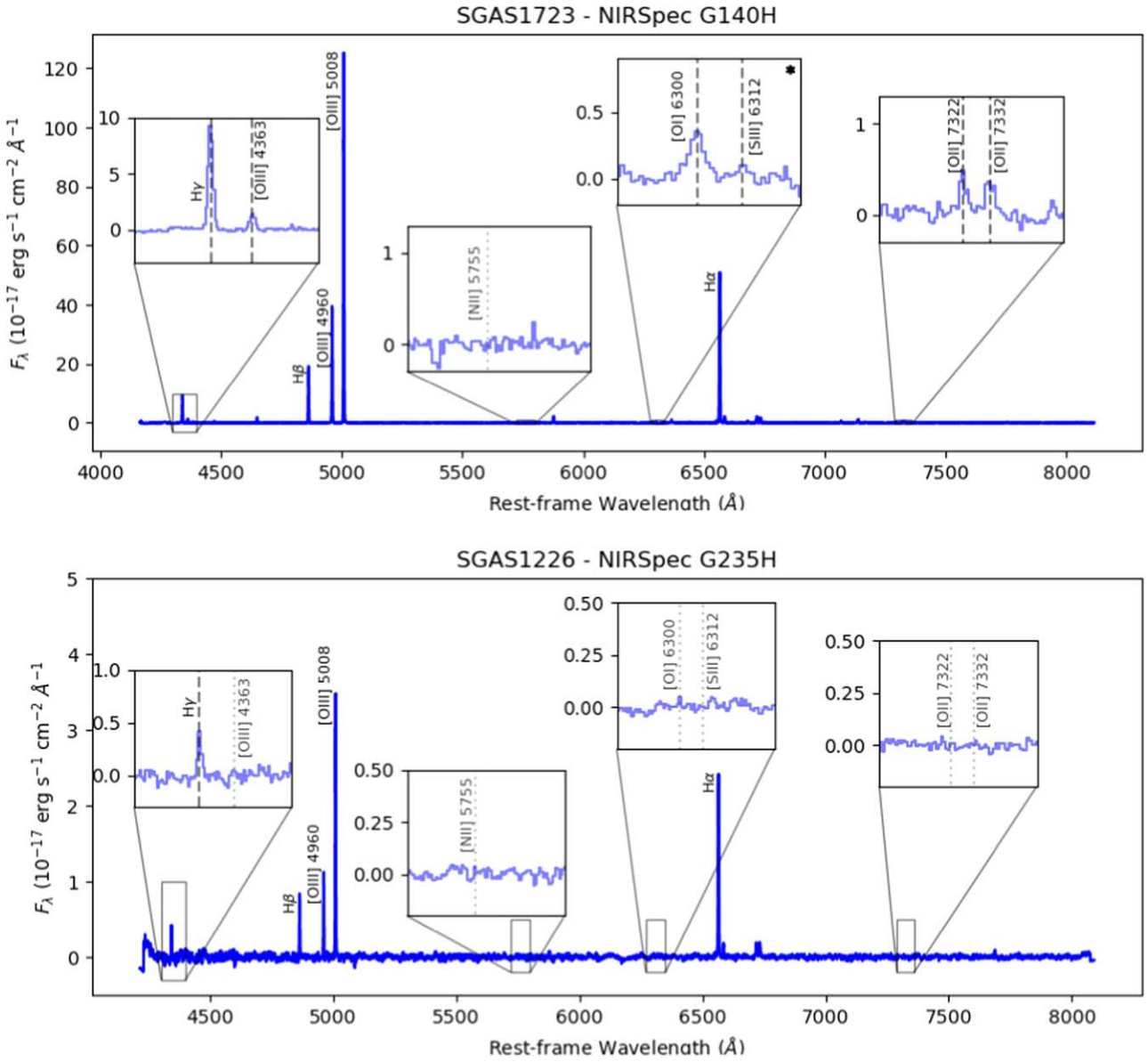

Figure 2. Top: continuum-subtracted NIRSpec spatially integrated spectrum of SGAS1723+34, with auroral line regions highlighted in zoomed insets. Three auroral lines are detected, while the fourth ([N II] λ5755) is not detected. The panel demarcated with an asterisk, containing [O I] λ6300 and [S III] λ6312, shows the spectrum integrated over a smaller aperture, selected to avoid excess noise from pixels at the detector edges (see the Appendix for details). Bottom: continuum-subtracted NIRSpec spatially integrated spectrum of SGAS1226+21, with auroral lines highlighted in zoomed insets. No auroral lines are detected in this target. In both panels, detected lines are marked with dashed lines, while nondetections are marked with dotted lines.

3.2. Emission-line Measurements

Line fitting for this paper was done using the JWST TEMPLATES repository of tools, which are publicly available on the TEMPLATES Github repository.[26] Notebooks used for line fitting and subsequent analysis are available at doi:10.5281/zenodo.13697056.[27] Measured line fluxes are reported in Table 1.

Significant continuum flux is detected for each of our target galaxies. To properly measure emission-line fluxes, we first measure and subtract the continuum flux for each source. This is done by first masking out all detected emission lines, then smoothing the remaining continuum using a boxcar convolution. The boxcar size for convolution is chosen to be 100 Å at the source redshift, and we assume a width of 300 km s^{-1} when masking out known emission lines. This width is chosen prior to fitting, and is intentionally broad to preserve line fluxes. Tests with different mask widths do not significantly change our line flux measurements. Wavelength ranges that have been masked due to the presence of emission lines are interpolated to provide a smooth estimate of the continuum across the full spectrum. The boxcar-smoothed, interpolated spectrum is our estimate of the source continuum level, and is subtracted from the original spectrum prior to fitting emission lines.

We fit the continuum-subtracted emission lines of each spectrum with Gaussian profiles using the `scipy curve_fit` function (P. Virtanen et al. 2020). Line fluxes are calculated by integrating the Gaussian profile. Uncertainties on the Gaussian width and amplitude are propagated to calculate the line flux uncertainties. Resolved neighboring emission lines

[26] https://github.com/JWST-Templates/jwst_templates
[27] https://github.com/bwelch94/templates-auroral-stacked/

Table 1
Emission-line Flux Measurements

Line	λ_{rest}	Flux (S1723)	Intensity $I(\lambda)$ (S1723)	Flux (S1226)	Intensity $I(\lambda)$ (S1226)
Hγ	4341.68	69.67 ± 0.97	84.89 ± 1.19	4.96 ± 0.53	8.78 ± 0.93
[O III] λ4363	4364.44	11.34 ± 1.07	13.80 ± 1.30	<0.46	<0.81
Hβ	4862.68	155.52 ± 3.42	184.49 ± 4.06	10.46 ± 0.50	17.12 ± 0.82
[O III] λ4960	4960.30	325.48 ± 3.83	384.43 ± 4.56	14.05 ± 0.54	22.72 ± 0.87
[O III] λ5008	5008.24	976.50 ± 5.66	1150.99 ± 6.85	46.35 ± 0.65	74.46 ± 1.04
[N II] λ5756	5756.24	<0.45	<0.51	<0.12	<0.19
[O I] λ6302	6302.05	4.09 ± 0.25	4.80 ± 0.30	0.00 ± 0.00	0.00 ± 0.00
[S III] λ6313	6313.80	0.91 ± 0.22[a]	1.07 ± 0.25[a]	<0.11	<0.16
[N II] λ6550	6549.85	5.74 ± 2.11	6.48 ± 2.38	0.77 ± 0.43	1.08 ± 0.61
Hα	6564.61	503.84 ± 3.79	568.09 ± 4.32	39.53 ± 0.64	55.88 ± 0.90
[N II] λ6585	6585.28	19.39 ± 2.11	21.85 ± 2.38	2.33 ± 0.47	3.29 ± 0.66
[S II] λ6718	6718.29	23.76 ± 1.08	26.70 ± 1.22	3.75 ± 0.32	5.24 ± 0.45
[S II] λ6733	6732.67	17.68 ± 1.07	19.85 ± 1.20	3.59 ± 0.33	5.02 ± 0.46
[Ar III] λ7138	7137.80	12.23 ± 0.87	13.61 ± 0.97	<0.13	<0.17
[O II] λ7322	7322.01	3.50 ± 0.45	3.88 ± 0.50	<0.09	<0.12
[O II] λ7332	7331.68	3.22 ± 0.38	3.57 ± 0.42	<0.09	<0.12

Notes. Emission-line flux measurements. Column (1): line identification. Column (2): rest-frame vacuum wavelength, in units of angstroms. Column (3): observed flux for SGAS1723+34, in units of 10^{-17} erg s^{-1} cm^{-2}. Column (4): dereddened intensity for SGAS1723+34, in units of 10^{-17} erg s^{-1} cm^{-2}. Column (5): observed flux for SGAS1226+21, in units of 10^{-17} erg s^{-1} cm^{-2}. Column (6): dereddened intensity for SGAS1226+21, in units of 10^{-17} erg s^{-1} cm^{-2}. 3σ upper limits are given for lines without clear detections.
[a] [S III] λ6312 is partially cut off by the detector gap in SGAS1723+34, thus this line is only measured for half of the galaxy.

(e.g., [O III] λ4959 and [O III] λ5007) and partially blended emission lines (e.g., [O II] $\lambda\lambda$7320, 7330) are fit simultaneously. The [O II] $\lambda\lambda$7320, 7330 doublet technically consists of four emission lines, with vacuum wavelengths 7320.94, 7322.01, 7331.68, and 7332.75 Å.[28] Due to the proximity of the ∼7320 Å doublet and the ∼7330 Å doublet, these lines are not resolved in the NIRSpec high resolution gratings. We therefore fit this feature with two Gaussians centered around 7320 and 7330 Å rest frame, allowing the wavelength centroids to vary within a flat prior of ±5 Å in the observed frame. The redshifts of the two lines are not fixed together, however we find that the best-fit redshifts are consistent within the 1σ uncertainties.

We do not fix any doublet line flux ratios while fitting, however we do confirm that our measured flux ratio for [O III] λ5007/[O III] λ4959 is consistent with the theoretical value given in P. J. Storey & C. J. Zeippen (2000). We do not generally fix line widths when fitting our emission lines. However, in the case of the faintest auroral lines, we fix the line widths to what have been measured from related strong lines from the same element, as these will trace the same gas. This only notably changes the [O II] $\lambda\lambda$7320, 7330 flux for SGAS1723+34. As this set of lines has a low SNR, the fitting function favors a wider Gaussian profile than other oxygen lines measured for this target, artificially driving up the flux of the line. We fix the [O II] $\lambda\lambda$7320, 7330 line widths to the mean velocity width measured from the bright [O III] $\lambda\lambda$4959, 5007 lines. We correct the width for the changing dispersion of the NIRSpec grating, using available dispersion files from the JWST documentation. We note that the [S III] λ6312 line has a similarly low SNR, however the best-fit line width matches the predicted line width based on the [S II] $\lambda\lambda$6717, 6731 line.

Prior to attempting to fit faint lines, we check if there is a significant excess of flux in the line region compared to the surrounding spectral regions. We first define a region of interest that would contain the emission line. Then we define a separate continuum region in the vicinity of the line region that we do not expect to contain any detectable emission or absorption features. We sum the flux densities within the line region. Then we calculate rolling sums of flux density in the continuum region, with the same width in wavelength as the line region (e.g., if the line region is 10 Å wide, we would calculate flux density sums in 10 Å bins centered on each resolution element within the continuum region). We calculate the median and standard deviation of these rolling flux measurements. If the line flux sum is less than 3σ above the median of the rolling fluxes, we consider the line to be undetected. It can be informative to set upper limits on undetected auroral lines. We set these upper limits at the 3σ level described above.

Visual inspection shows the [O III] λ4363 line may exist just below the detection limit in SGAS1226+21. We thus attempt a Gaussian fit despite this line being below our standard detection limit. This fit yields a flux of $0.45 \pm 0.53 \times 10^{-17}$ erg s^{-1} cm^{-2} Å^{-1}, just below our 3σ upper limit of 0.46×10^{-17} erg s^{-1} cm^{-2} Å^{-1}, albeit with large uncertainties. The large 1σ uncertainties from the attempted Gaussian fit are the result of insufficient signal to generate a reliable fit, thus we retain the upper limit calculated using the previously described rolling sum method as our preferred limit. Additional exposure time could reasonably detect this line in the future.

For the [S III] λ6312 line in SGAS1723+34, the method described above produces only an upper limit with the original full-galaxy spectrum. However, looking at the IFU data cube, it appears that a line is present at the expected wavelength, however it is partially cut off by the NIRSpec detector gap. We therefore perform a separate spectral extraction and local continuum subtraction in an effort to properly measure the flux of this line. This process is described in the Appendix. We report the flux measured in this smaller aperture with local continuum subtraction in Table 1, with an asterisk to denote the atypical measurement.

[28] Queried from NIST via https://linelist.pa.uky.edu/atomic/.

3.3. Temperature, Density, and Abundance Calculations

3.3.1. Extinction Correction

We first correct our measured emission-line fluxes for dust reddening, both from the Milky Way ISM and dust within the target galaxy. In both cases we use the extinction law of J. A. Cardelli et al. (1989). The Milky Way ISM reddening correction is made using a 3D dust map from G. M. Green et al. (2019), accessed through the `dustmaps` python package (G. Green 2018). At the position of SGAS1723+34, the Milky Way $E(B-V)=0.03$, while for SGAS1226+21, the Milky Way $E(B-V)=0.00$.

After accounting for Galactic reddening, we next correct for dust within the target galaxy using the ratios of Hα to Hβ and Hβ to Hγ. We first calculate a predicted Hα/Hβ and Hβ/Hγ ratios using PYNEB (V. Luridiana et al. 2015). This initial calculation assumes an electron temperature of 10^4 K and density of 100 cm^{-3}. The measured Hα/Hβ and Hβ/Hγ ratios are then compared to the predicted ratios to calculate the reddening correction. This reddening correction is then applied to our measured emission lines, and a new temperature and density are calculated using the [O III] λ4363/[O III] λ5007 and [S II] λ6717/[S II] λ6731 ratios, respectively. This process is repeated iteratively until the difference in temperature between iterations is less than 10 K. In the case of SGAS1226+21, no line is detected for [O III] λ4363. For this process, we treat the upper limit as a detection, iteratively measuring the temperature from the flux upper limit until the change is less than 10 K. This process results in reddening measurements of $E(B-V)=0.05\pm0.01$ for SGAS1723+34, and $E(B-V)=0.11\pm0.04$ for SGAS1226+21.

3.3.2. Electron Temperature and Density Calculations

For SGAS1723+34, we have detected the [O III] λ4363, [O II] $\lambda\lambda$7320, 7330, and [S III] λ6312 auroral emission lines, and placed an upper limit on the [N II] λ5755 auroral line. Meanwhile SGAS1226+21 has yielded only upper limits on each of these auroral lines. We calculate electron densities and temperatures from these emission-line measurements using the `PYNEB` function `getTemDen` (V. Luridiana et al. 2015).

We first calculate the electron density for each target using the [S II] λ6717/[S II] λ6731 line ratio, which is well detected in both galaxies and is sensitive to density. To account for uncertainties in line flux measurements, we randomly sample a Gaussian distribution with mean and standard deviation given by our line flux and flux uncertainty. We calculate the density using 300 samples, and use the median and standard deviation of the resulting distribution as our density and uncertainty. Below a density of $\sim$100 cm^{-3}, this ratio does not change considerably as a function of density (see, e.g., D. A. Berg et al. 2018). In the case of SGAS1723+34, we are in this regime, leading to an increased uncertainty in our density measurement. For this reason, we choose to use a fiducial density of 100 cm^{-3} for our temperature calculations. SGAS1226+21 is not in this low density regime, so we use our measured value of $\sim$600 cm^{-3} for future calculations.

We calculate electron temperature for the highly ionized gas from the [O III] λ4363/[O III] λ5007 line ratio. For the lower ionization gas we use the [O II] $\lambda\lambda$7320, 7330/[O II] $\lambda\lambda$3727, 3729 temperature sensitive line ratio. While we have a detection of [S III] λ6312, we do not have the wavelength coverage to measure [S III] $\lambda\lambda$9069, 9532, which is needed to calculate the electron temperature in the intermediate ionization zone. To estimate uncertainties on the temperature measurement, we randomly select line ratios from a Gaussian distribution with mean equal to the measured ratio and standard deviation equal to the uncertainty on the measured ratio. We use 300 points randomly sampled from this distribution. The physical quantity is then calculated for each sample. The median of the resulting distribution of physical parameters is taken as our final value, with the standard deviation providing the uncertainty on this value.

The [O II] $\lambda\lambda$7320, 7330 temperature calculation relies on a measurement of [O II] $\lambda\lambda$3727, 3729, which is outside the wavelength range of the JWST NIRSpec data for both targets. We thus use existing measurements from other observatories of this line for both targets. As described in Section 2, SGAS1723+34 has [O II] $\lambda\lambda$3727, 3729 fluxes measured by both the HST WFC3 grism and Keck ESI, reported in J. R. Rigby et al. (2021).

SGAS1226+21 has [O II] $\lambda\lambda$3727, 3729 blended flux observed by the Keck NIRSPEC instrument, reported in E. Wuyts et al. (2012). As discussed in Section 2, we rescale the reported [O II] $\lambda\lambda$3727, 3729 flux by the [O III] λ4959 flux, as the reported atmospheric transmission for these two lines is consistent for the ground-based data.

Finally, we apply our own reddening corrections to the rescaled observed fluxes obtained from the literature, as described in Section 3.3.1. This results in dereddened intensities of $I(\lambda3727)=109.0\pm0.8\times10^{-17}$ erg s^{-1} cm^{-2}, $I(\lambda3729)=153.4\pm0.8\times10^{-17}$ erg s^{-1} cm^{-2} for SGAS1723+34, and $I(\lambda\lambda3727,3729)=48\pm9\times10^{-17}$ erg s^{-1} cm^{-2} for SGAS1226+21.

Our upper limit on the electron temperature for O^+ in SGAS1226+21 is extremely low. Because this limit relies on the uncertain rescaling of the ground-based [O II] $\lambda\lambda$3727, 3729 line fluxes, we conclude that the extremely low O^+ temperature is likely erroneous. We include it here for completeness only.

Calculating a temperature from the [S III] λ6312 line requires a measurement of the [S III] $\lambda\lambda$9069, 9532 doublet, which falls outside the wavelength coverage of the JWST NIRSpec gratings obtained from TEMPLATES. We thus estimate the [S III] temperature using the relation from D. R. Garnett (1992):

$$T_e(S^{++}) = 0.83\ T_e(O^{++}) + 1700. \quad (1)$$

For [N II], we employ our upper limit to calculate a temperature based on the [N II] λ5755/[N II] $\lambda\lambda$6548, 6584 ratio limit. We then compare this value to the temperature estimated from $T_e(O^{++})$ using the relation from D. R. Garnett (1992):

$$T_e(N^{+}) = 0.7\ T_e(O^{++}) + 3000. \quad (2)$$

The D. R. Garnett (1992) temperature relations equate $T_e(O^+)=T_e(N^+)$. Our measured value for $T_e(O^+)$ is slightly higher than the value calculated based on the measured $T_e(O^{++})$, with a discrepancy of $\sim2\sigma$. Our measured $T_e(O^+)$ is also $\sim1.2\sigma$ greater than our upper limit on $T_e(N^+)$ from our nondetection of the [N II] λ5755 line. We thus choose to use the calculated value of $T_e(N^+)_{TT}$ for further calculations.

3.3.3. Abundance Calculations

We can use our measured electron temperatures to calculate direct elemental abundances within SGAS1723+34. For

SGAS1226+21 we only set an upper limit on the oxygen abundance, as no auroral lines are detected.

We primarily follow the atomic data recommendations laid out in Table 4 of D. A. Berg et al. (2015), with two exceptions. First, we use the updated transition probabilities of P. Rynkun et al. (2019) for S^{+}. Second, we use the collision strength data of K. M. Aggarwal & F. P. Keenan (1999) for O^{++}. We recalculate the UV diagnostics using archival emission-line strengths, however the collision data from P. J. Storey et al. (2014), recommended by D. A. Berg et al. (2015), do not cover the UV transitions (i.e., O III] $\lambda\lambda$1660, 1666). We therefore choose to use the collision data of K. M. Aggarwal & F. P. Keenan (1999) for consistent comparisons between results.

Ionic abundances relative to hydrogen are calculated using

$$\frac{\mathrm{N}(X^{i})}{\mathrm{N}(\mathrm{H}^{+})} = \frac{I_{\lambda(i)}}{I_{\mathrm{H}\beta}} \frac{j_{\mathrm{H}\beta}}{j_{\lambda(i)}}. \quad (3)$$

The emissivity coefficients $j_{\lambda(i)}$ are calculated with the relevant temperature and density measurements described above, using the `PYNEB` function `getIonAbundance` (V. Luridiana et al. 2015). As with the temperature and density measurements, we account for uncertainties by randomly sampling emission-line fluxes and electron temperatures from Gaussian distributions defined with mean equal to our measured flux/temperature, and standard deviation equal to the uncertainty on that parameter. We sample 300 iterations, and use the median and standard deviation of the resulting distribution to estimate the final abundance and uncertainty.

We use our measured $T_e(\mathrm{O}^{+})$ and $T_e(\mathrm{O}^{++})$ values to calculate the oxygen abundance, and we use $T_e(\mathrm{N}^{+})$ calculated using Equation (2) to estimate the nitrogen abundance for SGAS1723+34. We also use the upper limit on the N+ temperature to calculate a lower limit on the nitrogen abundance. This limit is consistent with our abundance calculated using Equation (2). We do not attempt to calculate a sulfur abundance, since we have neither a measurement of the electron temperature $T_e(\mathrm{S}^{++})$, nor a measurement of the [S III] $\lambda\lambda$9069, 9532 doublet. As mentioned earlier, an additional observation with the JWST NIRSpec G235H grating could measure the [S III] $\lambda\lambda$9069, 9532 doublet, enabling a measurement of the S^{++} electron temperature and direct measurement of the sulfur abundance.

For SGAS1226+21, we use our measured upper limit on $T_e(\mathrm{O}^{++})$ and the calculated limit on $T_e(\mathrm{O}^{+})$ using the empirical temperature relation of D. R. Garnett (1992) to calculate the total oxygen abundance. We do not attempt to extract limits on the abundance of other elements for this galaxy, as the requisite auroral lines are not detected.

We assume that the total oxygen abundance is given by $\mathrm{O/H} = \mathrm{O}^{+}/\mathrm{H}^{+} + \mathrm{O}^{++}/\mathrm{H}^{+}$. We do have a measurement of [O I] λ6300, which could provide a constraint on the abundance of oxygen in the lowest ionization state. However, the [O I] λ6300 line is partially cut off by the NIRSpec detector gap, and is not necessarily cospatial with the H II regions from which the other auroral lines and Balmer lines originate. We therefore choose not to include this line diagnostic because it only covers a small portion of the galaxy. Additionally, the contribution from [O I] is expected to be low. D. A. Berg et al. (2020) find that it contributes only 3% of the total oxygen abundance in their sample of local H II regions, corresponding to a total change of <0.02 dex, which is less than our measurement uncertainties.

We make the assumption that $\mathrm{N/O} \simeq \mathrm{N}^{+}/\mathrm{O}^{+}$, based on the similar ionization and excitation energies of these ions (M. Peimbert 1967). Previous work has found this to be valid within ~10% (A. Nava et al. 2006; A. Amayo et al. 2021). This assumption offers sufficient precision for the present analysis.

We use the ionization correction factor (ICF) presented in Y. I. Izotov et al. (2006) to calculate the total abundance of Ar/H for SGAS1723+34. Following their recommendations, we linearly interpolate between the "intermediate" and "high" metallicity ICF presented in Equation (22) of Y. I. Izotov et al. (2006), given our measured direct oxygen abundance falls in this range. The ionization energy of Ar^{++} overlaps both the intermediate and high-ionization zones. We choose to use the high-ionization temperature $T_e(\mathrm{O}^{++})$ when calculating the Ar^{++} abundance, since we have a direct measurement of $T_e(\mathrm{O}^{++})$.

4. Results and Discussion

4.1. Multiple Auroral Line Detections

We have measured fluxes for the auroral emission lines [O III] λ4363, [S III] λ6312, and [O II] $\lambda\lambda$7320, 7330 in the lensed galaxy SGAS1723+34, and set an upper limit on the [N II] λ5755 line flux. This is the second detection of the auroral [S III] λ6312 line published for an individual galaxy outside the local Universe after N. S. J. Rogers et al. (2024), suggesting that future JWST observations have a reasonable chance of detecting this feature in many more distant galaxies. We have set upper limits for each of the auroral lines for SGAS1226+21. Using these emission-line measurements, we have constrained the electron temperature and density within these two galaxies, and measured ionic abundances for SGAS1723+34. Our measured values are reported in Table 2.

Recently A. L. Strom et al. (2023) published deep, stacked spectra of $z \sim 2$–3 galaxies observed with JWST, including detections of three auroral lines: [N II] λ5755, [S III] λ6312, and [O II] $\lambda\lambda$7320, 7330. The authors present fluxes of these auroral lines as a percentage of Hα, offering a valuable comparison point for undetected lines in the present data. For SGAS1723+34, we find an upper limit for the undetected [N II] λ5755 line of $<4.5 \times 10^{-18}$ erg s^{-1} cm^{-2} (see Table 1). A. L. Strom et al. (2023) present a 68% confidence range of [N II] λ5755 percentages of Hα of [0.15–0.25]%. Applying this to our measured Hα flux, we find an expected 68% confidence range of $7.5-12.7 \times 10^{-18}$ erg s^{-1} cm^{-2}, which is greater than our measured upper limit. However, our measured [N II] λ6584/Hα ratio for SGAS1723+34 of $3.8\% \pm 0.4\%$ is about half that reported in A. L. Strom et al. (2023). If we assume that this is due to lower $\mathrm{N}^{+}/\mathrm{H}$ in SGAS1723+34 (either from lower N/H or higher ionization parameter relative to the CECILIA stack), the [N II] λ5755 line strength could fall by a similar margin at fixed electron temperature. This would bring the expected range to $3.8-6.4 \times 10^{-18}$ erg s^{-1} cm^{-2}, which is consistent with our measured upper limit on [N II] λ5755.

Our measured flux for [S III] λ6312 is consistent with the 68% confidence interval presented in A. L. Strom et al. (2023). For [S III] λ6312, our IFU data only cover one clump of the full lensed arc. Thus for accurate comparison, we calculate the Hα strength in that clump alone, finding a value of $212 \pm 2 \times 10^{-17}$ erg s^{-1} cm^{-2},

Table 2
Temperature and Abundance Measurements

Target	SGAS1723+34	SGAS1226+21
$T_e(O^{++})_{meas.}$ (K)	$12{,}200 \pm 400$	$<11{,}700$
$T_e(O^{+})_{meas.}$ (K)	$13{,}800 \pm 1000$	<5200 [a]
$T_e(N^{+})_{meas.}$ (K)	$<12{,}200$	$<22{,}400$
$n_{e,meas.}$ (cm^{-3})	110 ± 130	600^{+400}_{-300}
$n_{e,used}$ (cm^{-3})	100	600
$T_e(O^{+})_{TT}$ (K)	$11{,}600 \pm 300$	$<11{,}500$
$T_e(N^{+})_{TT}$ (K)	$11{,}600 \pm 300$	$<11{,}500$
$T_e(S^{++})_{TT}$ (K)	$11{,}800 \pm 300$	$<11{,}800$
O^{+}/H^{+}	$1.6 \pm 0.7 \times 10^{-5}$	$>2.2 \times 10^{-5}$
O^{++}/H^{+}	$1.20 \pm 0.12 \times 10^{-4}$	$>8.6 \times 10^{-5}$
N^{+}/H^{+}	$>1.5 \times 10^{-6}$	⋯
N^{+}/H^{+}_{TT}	$1.7 \pm 0.2 \times 10^{-6}$	⋯
log(N/O)	>-1.01	⋯
$\log(N/O)_{TT}$	-0.95 ± 0.2	⋯
Ar^{++}/H^{+}	$4.2 \pm 0.4 \times 10^{-7}$	⋯
ICF(Ar)	1.20 ± 0.12	⋯
Ar/H	$5.0 \pm 0.7 \times 10^{-7}$	⋯
log(Ar/O)	-2.43 ± 0.08	⋯
12 + log(O/H) (Direct)	8.13 ± 0.03	>8.04
12 + log(O/H) (N2Hα)	8.44 ± 0.06	8.22 ± 0.06
12 + log(O/H) (R23)	8.42 ± 0.09	8.45 ± 0.12

Notes. Electron temperatures, densities, and abundances calculated for both targets. Measured temperatures ($T_e(X)_{meas.}$) are calculated from detected auroral lines. Upper limits are derived from undetected auroral lines. Temperatures denoted $_{TT}$ are calculated from $T_e(O^{++})_{meas.}$ using the empirical relations of D. R. Garnett (1992). Abundance measurements denoted $_{TT}$ are calculated using the relevant $T_e(X)_{TT}$ temperatures.
[a] This temperature limit relies on an uncertain rescaling of ground-based [O II] λλ3727, 3729 flux measurements, and is likely too restrictive. We include it here for completeness only.

giving a ratio of [S III] λ6312/Hα of $0.4\% \pm 0.1\%$. This is consistent with the range measured by A. L. Strom et al. (2023).

Our measurement of [O II] λλ7320, 7330 is slightly below the range given in A. L. Strom et al. (2023). We find [O II] ratios of $0.69\% \pm 0.09\%$ and $0.64\% \pm 0.08\%$ for the blue and red lines, respectively. The other existing measurements of [O II] λλ7320, 7330 outside the local Universe come from R. L. Sanders et al. (2023, 2024). Both of these studies present line strengths which are ∼1.5%−2% of Hα in a total of four galaxies, slightly above of the range presented in A. L. Strom et al. (2023). Together, these measurements highlight the range of abundances present in galaxies at Cosmic Noon.

For SGAS1226+21, we did not detect auroral lines. We set upper limits on the line strengths and use those upper limits to calculate upper limits on electron temperature, but do not attempt a direct metallicity measurement. We compare our measured upper limits to the ranges seen in other Cosmic Noon galaxies from A. L. Strom et al. (2023). For [O II] λλ7320, 7330, we calculate expected 1σ lower limit line fluxes of 4.4×10^{-18} and 3.5×10^{-18} erg s^{-1} cm^{-2}, respectively. These expected values are brighter than our measured upper limits of 0.9×10^{-18} erg s^{-1} cm^{-2}. Similarly, for [S III] λ6312, we find a 1σ lower limit expected value of 1.2×10^{-18} erg s^{-1} cm^{-2}, slightly brighter than our upper limit of 1.1×10^{-18} erg s^{-1} cm^{-2}. This indicates that we might have expected to detect these lines. The fact that we do not detect these auroral lines indicates that this galaxy may be at a somewhat lower temperature (and thus higher metallicity) than expected based on strong-line diagnostics.

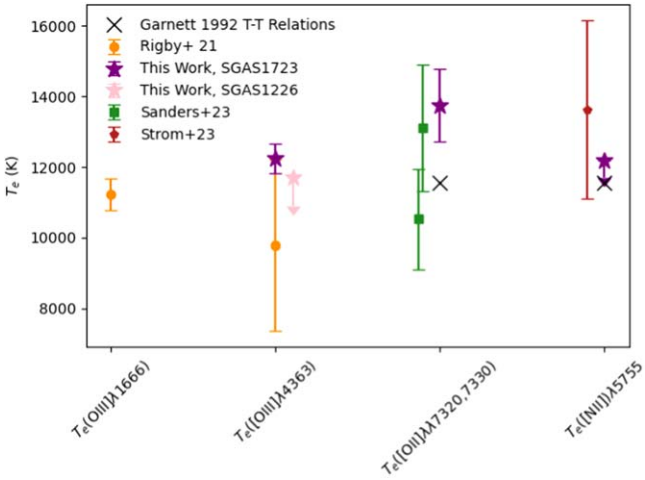

Figure 3. Electron temperatures from auroral line diagnostics for SGAS1723+34 are plotted as purple stars. SGAS1226+21 does not have detected auroral lines; instead, an upper limit for the [O III] temperature is plotted as a pink star. Comparison to J. R. Rigby et al. (2021) measurements for SGAS1723+34 are shown as yellow circles, along with a calculation of the [O II] and [N II] temperatures from the [O III] temperature, using the temperature relations of D. R. Garnett (1992). While SGAS1723+34 has a detection of [S III] λ6312, we do not have an available measurement of [S III] λλ9069, 9532, which is needed to make a temperature measurement. Other high-redshift O+ and N+ temperature measurements are shown from R. L. Sanders et al. (2023) at $z \sim 2$ (green squares) and from the stacked sample of A. L. Strom et al. (2023) at $z = 2$–3 (red pentagon). Our measured temperatures are consistent with these other high-redshift measurements.

4.2. Electron Temperatures of Multiple Ionization Zones

We use the auroral line flux measurements and upper limits to calculate electron temperatures. We compare our results for SGAS1723+34 to previously published temperature measurements from J. R. Rigby et al. (2021), as plotted in Figure 3. We recomputed the literature temperatures based on the reported measured line fluxes with our reddening correction applied, and using the same atomic data as in our temperature calculations for consistency. Our temperature measurement with the [O III] λ4363 line diagnostic is consistent with the literature value within the 1σ uncertainties. We also find that our measured temperature is consistent with the O III] λλ1660, 1666 diagnostic previously published within 1σ. The key improvement from the TEMPLATES data is the significant reduction in uncertainties. The [O III] λ4363 temperature uncertainty has been reduced by a factor of 6. This highlights the unique of JWST to deliver precise electron temperature diagnostics with modest observing time requirements.

A. L. Strom et al. (2023) only report the temperature for the low-ionization gas, based on the [N II] λ5755 line. Our measured upper limit on $T_e(N^{+}) < 12{,}300$ is consistent with their stacked value ($T_e = 13{,}630 \pm 2540$ K). Our measured [N II] λ5755 flux limit is low compared to their sample, however we also find a lower [N II] λ6548 flux. When the difference in [N II] λ6548 is accounted for, this discrepancy disappears.

The only other high-redshift temperature measurements for low-ionization O^{+} comes from R. L. Sanders et al. (2023, 2024).

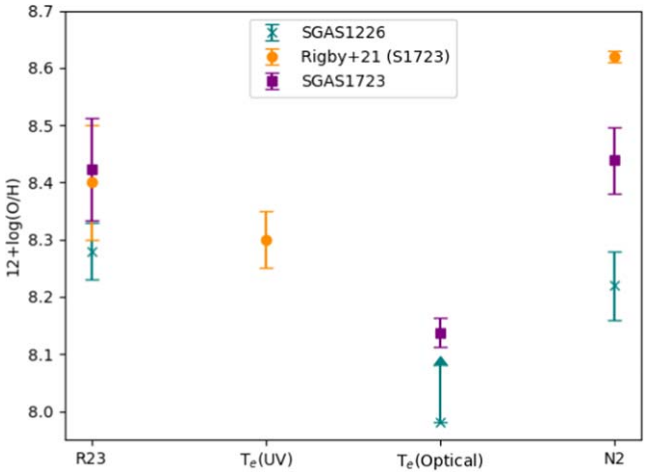

Figure 4. Oxygen abundance measurements $12 + \log(\mathrm{O/H})$ from both temperature and strong-line diagnostics. The direct-temperature-based measurement shown for SGAS1226+21 is a lower limit, as no auroral lines are clearly detected in that target. For SGAS1723+34, the direct abundance measurement is 0.3 dex lower than the strong-line diagnostics. The strong-line diagnostics R23 and N2 are self-consistent for both targets. Note that the direct abundance from J. R. Rigby et al. (2021) utilizes the temperature measured from O III] $\lambda\lambda$1660, 1666, which is likely the cause of the offset with our measurement based on [O III] λ4363.

Their temperatures are consistent with our measured $T_e(\mathrm{O}^+)$ within the uncertainties.

4.3. Oxygen Abundances from Direct and Strong-line Methods

Using our measurements of the electron temperature from the [O III] λ4363 and [O II] $\lambda\lambda$7320, 7330 lines, we measure a direct metallicity for SGAS1723+34 of $12 + \log(\mathrm{O/H}) = 8.15 \pm 0.03$. This value is $\sim$0.15 dex below the direct oxygen abundance reported in J. R. Rigby et al. (2021), which is based on the O III] $\lambda\lambda$1660, 1666 line. Dust will effect the UV lines more significantly than the optical, which could cause the discrepancy in these two abundance results. Our estimate of the dust reddening correction in this galaxy is $E(B-V) = 0.05 \pm 0.01$, as described in Section 3.3.1. To test if dust could plausibly cause the observed offset, we artificially increased the reddening correction iteratively until the two measurements were consistent within the uncertainties. We find that a value of $E(B-V) \sim 0.076$ brings the UV and optical measurements into agreement within the uncertainties, 2.6σ greater than our measured value. The shape of the reddening curve in the UV carries additional uncertainty. Repeating the reddening correction test with the reddening curve of E. L. Fitzpatrick (1999) yields a value of $E(B-V) = 0.07$ to get consistent UV and optical abundance results. Meanwhile, the curve of K. A. Misselt et al. (1999), measured from the Large Magellanic Cloud, gives $E(B-V) = 0.065$ with consistent UV and optical abundances, within 1.5σ of our measured reddening. We thus conclude that the observed offset is likely due to systematic uncertainty in the UV reddening correction.

We also computed the metallicity based on strong-line diagnostics, namely R23 (R23 = {[O II] $\lambda\lambda$3727, 3729 + [O III] $\lambda\lambda$4959, 5007}/Hβ) and N2 (N2 = [N II] λ6584/Hα). These bright line indicators are plotted in Figure 4 along with the direct measurements from this work and J. R. Rigby et al. (2021). The R23 diagnostic gives an oxygen abundance $12 + \log(\mathrm{O/H}) = 8.42 \pm 0.09$ for SGAS1723+34, using the relation presented in L. J. Kewley et al. (2019). The R23 abundance estimate is higher than the direct method abundance ($12 + \log(\mathrm{O/H}) = 8.14 \pm 0.03$) by $\sim$0.3 dex, however our R23 abundance is consistent with the R23 abundance calculated in J. R. Rigby et al. (2021). Discrepancies between the direct and strong-line abundances have been noted previously (e.g., G. Stasińska 2005; L. J. Kewley & S. L. Ellison 2008; Á. López-Sánchez et al. 2012). The R23 indicator notably has two possible branches in many formulations, which could explain the discrepancy seen here. For example, the lower branch presented in C. Ly et al. (2016) gives a metallicity of $12 + \log(\mathrm{O/H}) \sim 8.15$, consistent with our direct measurement. Meanwhile the higher branch of that same paper gives a metallicity of $12 + \log(\mathrm{O/H}) \sim 8.45$, consistent with our strong-line diagnostics. Another possible cause could be evolution with redshift, which P. Garg et al. (2024) suggest could be driven by redshift evolution of the ionization parameter. While the L. J. Kewley et al. (2019) relation attempts to correct for ionization parameter, the effect of redshift evolution on metallicity indicators will require additional study.

Our N2 metallicity indicator gives an oxygen abundance of $12 + \log(\mathrm{O/H}) = 8.44 \pm 0.06$ using the relation of L. J. Kewley et al. (2019), consistent with our measurement from R23. The N2 metallicity calculated in J. R. Rigby et al. (2021) is higher than our measurement by $\sim$0.2 dex. The N2 metallicity indicator in that paper was calculated from Gemini GNIRS data that only covered a small portion of the full arc. This minimal spatial coverage could be contributing to the offset between that work and our result. Interestingly, using the empirical calibration in Equation (1) of M. Pettini & B. E. J. Pagel (2004) gives an N2 metallicity measurement of $12 + \log(\mathrm{O/H}) = 8.09 \pm 0.03$, consistent with our direct measurement within the uncertainties.

M. Curti et al. (2017) note that at higher metallicities (starting around $12 + \log(\mathrm{O/H}) \approx 8.3$), contamination from the [Fe II] λ4360 line can artificially inflate the measured [O III] λ4363 flux, decreasing the inferred direct metallicity. We test for any contribution from [Fe II] λ4360 by including it as an extra component in fitting the [O III] λ4363 line. We find that the [Fe II] λ4360 component fits to zero flux, indicating that the [O III] λ4363 line flux is not contaminated. Further, we see no evidence of other iron lines present in the spectrum, indicating that [Fe II] λ4360 contamination is unlikely for this source.

We also calculate strong-line oxygen abundance diagnostics for SGAS1226+21, which are reported in Table 2, and shown in Figure 4. These metallicity values are consistent with previous estimates (E. Wuyts et al. 2012; A. Saintonge et al. 2013). Our metallicity from R23 is slightly higher than what we measure from N2, though the two are consistent within 2σ. The discrepancy is likely due to systematic effects introduced from attempting to match the archival Keck NIRSPEC data to the JWST NIRSpec IFU data. The N2 diagnostic utilizes only the JWST data, making that the more reliable metallicity indicator in this case. The lack of detected auroral lines prevents us from measuring the metallicity via the direct method for SGAS1226+21. However, we can set a lower limit of $12 + \log(\mathrm{O/H}) \geqslant 8.04$, less than and thus consistent with our strong-line measurements. As mentioned previously, the [O III] λ4363 line may be just below the detection threshold for the current observations. Deeper data covering this feature could plausibly yield a detection in the future.

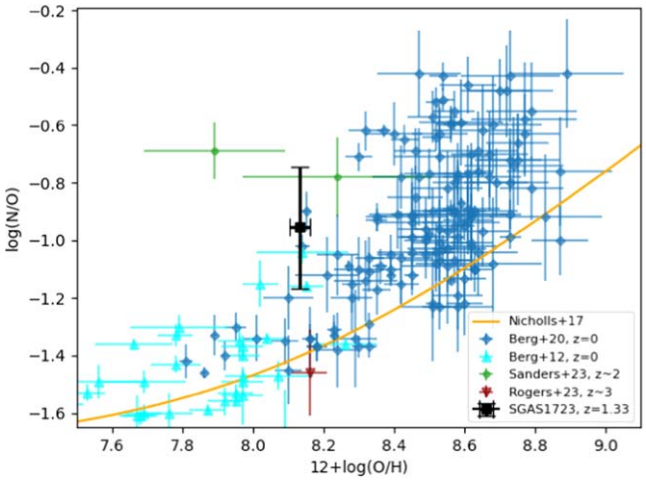

Figure 5. N/O vs. O/H from temperature-based abundance measures is plotted for SGAS1723+34 (black square), alongside local H II regions (D. A. Berg et al. 2020, blue diamonds), local dwarf galaxies (D. A. Berg et al. 2012, cyan triangles), and the nebular scaling relation calculated in D. C. Nicholls et al. (2017, orange line). Other high-redshift points from R. L. Sanders et al. (2023) are demarcated with green circles, and from N. S. J. Rogers et al. (2024) with a red triangle. The nitrogen abundance for SGAS1723+34 is calculated using the O^{++} electron temperature (see Section 3.3.3). Our measurement of the N/O ratio is consistent with local observations of star-forming galaxies, though we cannot rule out enhanced nitrogen abundance with our current uncertainties.

4.4. Nitrogen Enrichment

For SGAS1723+34, we calculate the direct nitrogen abundance. We do this in two ways, first using the calculated upper limit on the [N II] λ5755 line, and second using the O^{++} temperature calculated from the [O III] λ4363 line using Equation (2). We report both N^+/H^+ abundance estimates in Table 2. We find that the upper limit set by our nondetection of [N II] λ5755 is slightly lower (1.2σ) than the measured O^+ temperature. While there is considerable scatter in the $T_e(N^+)$–$T_e(O^+)$ relation in local galaxies, D. A. Berg et al. (2020) find that the oxygen temperatures are typically slightly higher ($\sim$1000−2000 K) than the nitrogen temperatures. Our measurements are consistent with this picture. We use the O^{++} temperature and Equation (2) to estimate the low-ionization electron temperature for our calculations of the nitrogen abundance. While the O^+ temperature offers a direct probe of the low-ionization electron temperature, this diagnostic is subject to several major systematic uncertainties in this study. The ratio of [O II] $\lambda\lambda$3727, 3729/[O II] $\lambda\lambda$7320, 7330 is strongly dependent on the reddening correction. In this case, the [O II] $\lambda\lambda$3727, 3729 and [O II] $\lambda\lambda$7320, 7330 lines are measured by different instruments, adding an additional source of systematic uncertainty. Deeper observations would be needed to detect the [N II] λ5755 line and refine these nitrogen abundance measurements.

As a consistency check, we calculate the N/O abundance using our measured O^+ temperature. We find that the $N/O(T_e(O^+)) = -1.1 \pm 0.2$, consistent with our quoted value using Equation (2) within the 1σ uncertainties.

We calculate the total N/O ratio as discussed in Section 3.3.3. We compare the N/O ratio for SGAS1723+34 to local H II regions from D. A. Berg et al. (2020), as well as nearby ($z \sim 0$) galaxies from D. A. Berg et al. (2012) in Figure 5, and find that this target is consistent with local measurements. Our measurement is also slightly higher than the scaling relation for gaseous nebulae calculated by D. C. Nicholls et al. (2017), though still within 2σ.

Interestingly, some previous measurements of N/O in $z \sim 2$ galaxies have shown significantly elevated nitrogen abundances compared to local galaxies (R. L. Sanders et al. 2023), while another measurement of a galaxy at $z \sim 3$ has shown a nitrogen abundance consistent with $z \sim 0$ galaxies (N. S. J. Rogers et al. 2024). While a number of factors could influence the elevated nitrogen abundances of the galaxies studied in R. L. Sanders et al. (2023), factors such as a top-heavy stellar initial mass function, leading to a larger number of Wolf–Rayet stars shedding nitrogen into the ISM, have been proposed to generate this large amount of nitrogen quickly (e.g., R. B. C. Henry et al. 2000; J. Brinchmann et al. 2008; C. Kobayashi & A. Ferrara 2024). An alternative explanation suggests that inflowing low-metallicity gas can dilute the oxygen abundance, driving increased N/O without requiring the presence of Wolf–Rayet stars (e.g., J. Köppen & G. Hensler 2005; R. O. Amorín et al. 2010; B. H. Andrews & P. Martini 2013).

We see no compelling evidence for this increased nitrogen fraction in SGAS1723+34, though we note that the best-fit value of log(N/O) does fall at the high end of the range seen in $z \sim 0$ galaxies reported in D. A. Berg et al. (2012). A detection of the [N II] λ5755 line would improve the measurement of N/O for this galaxy and clarify whether the nitrogen abundance is discrepant compared to $z \sim 0$ low-metallicity galaxies. Ultimately a larger sample of direct chemical abundance measurements will be needed in order to ascertain whether the overabundance of nitrogen in distant galaxies is typical or unusual. Additionally, we note that a variety of systematic effects could be influencing the observed discrepancies in these $z \sim 1$–3 galaxies. For example, R. L. Sanders et al. (2023) use the [O II] $\lambda\lambda$7320, 7330 lines as their primary temperature diagnostic for the low-ionization gas, while this study and N. S. J. Rogers et al. (2024) use the [O III] λ4363 line and the relation of D. R. Garnett (1992) to calculate the low-ionization gas temperature. Larger self-similar samples will help to determine the history of nitrogen synthesis in galaxies.

4.5. Ar/O Abundance

We detect the [Ar III] λ7138 line for SGAS1723+34, allowing us to make a direct measurement of the Ar/H abundance, as well as the ratio of Ar/O. As reported in Table 2, we find an Ar/O ratio of $\log(Ar/O) = -2.44 \pm 0.07$, consistent with the solar abundance $\log(Ar/O) = -2.37 \pm 0.11$ (M. Asplund et al. 2021).

Recently, N. S. J. Rogers et al. (2024) reported a direct Ar/O abundance of $\log(Ar/O) = -2.71 \pm 0.09$ at $z \sim 3$, noting that this is significantly lower than the solar abundance. They use this measurement to argue that this galaxy has been enriched mainly by core-collapse supernovae, as fewer Type Ia supernovae would have time to develop by $z \sim 3$. Our measurement for SGAS1723+34 being consistent with solar Ar/O abundance suggests that it is further along in its evolution, such that enough time has elapsed for enrichment by Type Ia supernovae. Additional direct argon abundance measurements at high z will provide further nuance to the buildup of α-elements over cosmic time.

5. Conclusions

We report the detection of multiple auroral lines in the gravitationally lensed galaxy SGAS1723+34 ($z = 1.3292$). Using these lines, we calculate the temperature of both the high- and low-ionization regions of oxygen gas, finding $T_e \sim 12{,}000$ K in both regions. These temperatures enable calculation of the total oxygen abundance via the direct method, yielding a value of $12 + \log(\mathrm{O/H}) = 8.15 \pm 0.03$. We also use the low-ionization temperature to calculate the nitrogen abundance in this galaxy, finding it is consistent with local H II regions. We do not detect auroral line emission in the lensed galaxy SGAS1226+21.

This study focused on the coadded spectra, collapsing all of the information from these lensed galaxies into a single spectrum to maximize the SNR. The TEMPLATES NIRSpec IFU observations present an opportunity to spatially resolve these emission lines. Analysis of the spatially resolved abundances in SGAS1723+34 will be presented in a forthcoming companion paper (G. M. Olivier et al. 2024, in preparation).

Acknowledgments

We thank Allison Strom and Gwen Rudie of the CECILIA team for collegial discussions that strengthened this paper. This work was based on observations taken with the NASA/ESA/CSA JWST. JWST is operated by the Space Telescope Science Institute under the management of the Association of Universities for Research in Astronomy, Inc., under NASA contract no. NAS 5-03127. These observations were taken as part of JWST DD-ERS program 1355. The JWST data analyzed in this paper were obtained from the Mikulski Archive for Space Telescopes (MAST) at the Space Telescope Science Institute. The specific observations analyzed can be accessed via doi:10.17909/e9p4-xm44. Support for JWST program 1355 was provided by NASA through a grant from the Space Telescope Science Institute, which is operated by the Association of Universities for Research in Astronomy, Inc., under NASA contract NAS 5-03127. B.W. acknowledges support from NASA under grant No. 80GSFC21M0002.

Facility: JWST.

Software: astropy (Astropy Collaboration et al. 2013, 2018, 2022), scipy (P. Virtanen et al. 2020), and matplotlib (J. D. Hunter 2007).

Appendix
Measuring the [S III] Auroral Line Flux with Local Continuum Subtraction

As mentioned in Section 3.2, the [S III] λ6312 line produces only an upper limit on the flux when using our standard continuum subtraction and line fitting procedure in SGAS1723+34. However, visual inspection of the IFU data cube reveals that an emission line is present at the expected wavelength. This line is only partially visible due to the NIRSpec detector gap. The lack of an apparent emission line in the final coadded spectrum is due to increased noise from detector edge pixels within our spectral extraction aperture.

In an effort to recover a line flux for [S III] λ6312, we create a partial extraction aperture that avoids the noisy detector edge pixels, as outlined in green in Figure 6. This follows our regular aperture along the southern portion of the arc for consistency with our other measurements. We make no attempt to correct the flux for the fact that only part of the galaxy is observed, since we do not have the [S III] $\lambda\lambda$9069, 9532 lines required to make a temperature measurement for [S III]. If future observations measure the [S III] $\lambda\lambda$9069, 9532 lines, a more detailed treatment of this line flux will be warranted.

To measure the [S III] λ6312 line flux, we employ a local continuum subtraction technique using `specutils`. We select continuum regions bracketing the [O I] λ6300 and [S III] λ6312 lines, as shown in Figure 6. This process preserves the flux of the [S III] λ6312 line, and allows us to fit it with a Gaussian rather than merely setting an upper limit. We report this flux in Table 1.

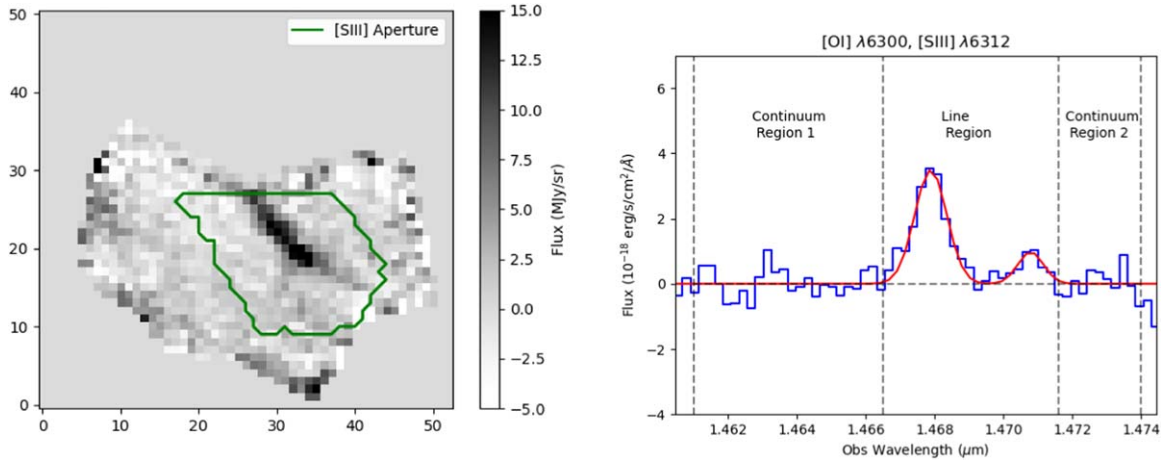

Figure 6. The auroral [S III] λ6312 line appears near the NIRSpec detector gap in observations of SGAS1723+34, causing only part of the arc to be visible. The left panel shows a sum of 10 IFU cube slices centered on [S III] λ6312, in the JWST pipeline units of MJy sr^{-1}. Because the edge spaxels tend to be noisier than others, we use a smaller extraction aperture (green line) to measure the flux of this line that avoids unnecessary edge spaxels. The resulting continuum-subtracted spectrum is shown in the right panel (blue line). We use a local continuum fitting technique for this line, utilizing two continuum regions adjacent to the emission lines of interest. Our fit to the [O I] λ6300 and [S III] λ6312 lines is shown in red. This method gives us the most reliable flux measurement for this faint auroral line on the edge of the detectors.

ORCID iDs

Brian Welch https://orcid.org/0000-0003-1815-0114
Grace M. Olivier https://orcid.org/0000-0002-4606-4240
Taylor A. Hutchison https://orcid.org/0000-0001-6251-4988
Jane R. Rigby https://orcid.org/0000-0002-7627-6551
Danielle A. Berg https://orcid.org/0000-0002-4153-053X
Manuel Aravena https://orcid.org/0000-0002-6290-3198
Matthew B. Bayliss https://orcid.org/0000-0003-1074-4807
Jack E. Birkin https://orcid.org/0000-0002-3272-7568
Scott C. Chapman https://orcid.org/0000-0002-8487-3153
Håkon Dahle https://orcid.org/0000-0003-2200-5606
Michael D. Gladders https://orcid.org/0000-0003-1370-5010
Gourav Khullar https://orcid.org/0000-0002-3475-7648
Keunho J. Kim https://orcid.org/0000-0001-6505-0293
Guillaume Mahler https://orcid.org/0000-0003-3266-2001
Matthew A. Malkan https://orcid.org/0000-0001-6919-1237
Desika Narayanan https://orcid.org/0000-0002-7064-4309
Kedar A. Phadke https://orcid.org/0000-0001-7946-557X
Keren Sharon https://orcid.org/0000-0002-7559-0864
J. D. T. Smith https://orcid.org/0000-0003-1545-5078
Manuel Solimano https://orcid.org/0000-0001-6629-0379
Justin S. Spilker https://orcid.org/0000-0003-3256-5615
Joaquin D. Vieira https://orcid.org/0000-0001-7192-3871
David Vizgan https://orcid.org/0000-0001-7610-5544

References

Aggarwal, K. M., & Keenan, F. P. 1999, ApJS, 123, 311
Amayo, A., Delgado-Inglada, G., & Stasińska, G. 2021, MNRAS, 505, 2361
Amorín, R. O., Pérez-Montero, E., & Vílchez, J. M. 2010, ApJL, 715, L128
Andrews, B. H., & Martini, P. 2013, ApJ, 765, 140
Arellano-Córdova, K. Z., Berg, D. A., Chisholm, J., et al. 2022, ApJL, 940, L23
Asplund, M., Amarsi, A. M., & Grevesse, N. 2021, A&A, 653, A141
Astropy Collaboration, Price-Whelan, A. M., Lim, P. L., et al. 2022, ApJ, 935, 167
Astropy Collaboration, Price-Whelan, A. M., Sipőcz, B. M., et al. 2018, AJ, 156, 123
Astropy Collaboration, Robitaille, T. P., Tollerud, E. J., et al. 2013, A&A, 558, A33
Berg, D. A., Erb, D. K., Auger, M. W., Pettini, M., & Brammer, G. B. 2018, ApJ, 859, 164
Berg, D. A., Pogge, R. W., Skillman, E. D., et al. 2020, ApJ, 893, 96
Berg, D. A., Skillman, E. D., Croxall, K. V., et al. 2015, ApJ, 806, 16
Berg, D. A., Skillman, E. D., Marble, A. R., et al. 2012, ApJ, 754, 98
Birkin, J. E., Hutchison, T. A., Welch, B., et al. 2023, ApJ, 958, 64
Böker, T., Beck, T. L., Birkmann, S. M., et al. 2023, PASP, 135, 038001
Brinchmann, J. 2023, MNRAS, 525, 2087
Brinchmann, J., Kunth, D., & Durret, F. 2008, A&A, 485, 657
Bushouse, H., Eisenhamer, J., Dencheva, N., et al. 2023, JWST Calibration Pipeline, v1.11.4, Zenodo, doi:10.5281/zenodo.8247246
Cardelli, J. A., Clayton, G. C., & Mathis, J. S. 1989, ApJ, 345, 245
Casey, C. M., Narayanan, D., & Cooray, A. 2014, PhR, 541, 45
Christensen, L., Laursen, P., Richard, J., et al. 2012, MNRAS, 427, 1973
Croxall, K. V., Pogge, R. W., Berg, D. A., Skillman, E. D., & Moustakas, J. 2015, ApJ, 808, 42
Croxall, K. V., Pogge, R. W., Berg, D. A., Skillman, E. D., & Moustakas, J. 2016, ApJ, 830, 4
Curti, M., Cresci, G., Mannucci, F., et al. 2017, MNRAS, 465, 1384
Curti, M., Dugenio, F., Carniani, S., et al. 2023, MNRAS, 518, 425
Dinerstein, H. L. 1990, in The Interstellar Medium in Galaxies (Astrophysics and Space Science Library) ed. J. Thronson & J. Thronson, Vol. 161 (Dordrecht: Kluwer), 257
Fitzpatrick, E. L. 1999, PASP, 111, 63
Florian, M. K., Rigby, J. R., Acharyya, A., et al. 2021, ApJ, 916, 50
Gardner, J. P., Mather, J. C., Abbott, R., et al. 2023, PASP, 135, 068001
Garg, P., Narayanan, D., Sanders, R. L., et al. 2024, ApJ, 972, 113
Garnett, D. R. 1992, AJ, 103, 1330
Green, G. 2018, JOSS, 3, 695
Green, G. M., Schlafly, E., Zucker, C., Speagle, J. S., & Finkbeiner, D. 2019, ApJ, 887, 93
Henry, R. B. C., Edmunds, M. G., & Köppen, J. 2000, ApJ, 541, 660
Hunter, J. D. 2007, CSE, 9, 90
Hutchison, T. A., Welch, B. D., Rigby, J. R., et al. 2024, PASP, 136, 044503
Izotov, Y. I., Stasińska, G., Meynet, G., Guseva, N. G., & Thuan, T. X. 2006, A&A, 448, 955
James, B. L., Pettini, M., Christensen, L., et al. 2014, MNRAS, 440, 1794
Katz, H., Saxena, A., Cameron, A. J., et al. 2023, MNRAS, 518, 592
Kewley, L. J., & Ellison, S. L. 2008, ApJ, 681, 1183
Kewley, L. J., Nicholls, D. C., & Sutherland, R. S. 2019, ARA&A, 57, 511
Kobayashi, C., & Ferrara, A. 2024, ApJL, 962, L6
Koester, B. P., Gladders, M. D., Hennawi, J. F., et al. 2010, ApJL, 723, L73
Köppen, J., & Hensler, G. 2005, A&A, 434, 531
Kubo, J. M., Allam, S. S., Drabek, E., et al. 2010, ApJL, 724, L137
López-Sánchez, Á., Dopita, M. A., Kewley, L. J., et al. 2012, MNRAS, 426, 2630
Luridiana, V., Morisset, C., & Shaw, R. A. 2015, A&A, 573, A42
Ly, C., Malkan, M. A., Rigby, J. R., & Nagao, T. 2016, ApJ, 828, 67
Ly, C., Rigby, J. R., Cooper, M., & Yan, R. 2015, ApJ, 805, 45
Misselt, K. A., Clayton, G. C., & Gordon, K. D. 1999, ApJ, 515, 128
Nava, A., Casebeer, D., Henry, R. B. C., & Jevremovic, D. 2006, ApJ, 645, 1076
Nicholls, D. C., Sutherland, R. S., Dopita, M. A., Kewley, L. J., & Groves, B. A. 2017, MNRAS, 466, 4403
Peimbert, M. 1967, ApJ, 150, 825
Pettini, M., & Pagel, B. E. J. 2004, MNRAS, 348, L59
Pontoppidan, K. M., Barrientes, J., Blome, C., et al. 2022, ApJL, 936, L14
Rauscher, B. J. 2024, PASP, 136, 015001
Rhoads, J. E., Wold, I. G. B., Harish, S., et al. 2023, ApJL, 942, L14
Rigby, J., Hutchison, T. A., Rivera-Thorsen, T. E., et al. 2024, JWST-Templates/Notebooks v1.0.2 Zenodo, doi:10.5281/zenodo.10933642
Rigby, J., Perrin, M., McElwain, M., et al. 2023a, PASP, 135, 048001
Rigby, J. R., Florian, M., Acharyya, A., et al. 2021, ApJ, 908, 154
Rigby, J. R., Vieira, J. D., Phadke, K. A., et al. 2023b, arXiv:2312.10465
Rogers, N. S. J., Strom, A. L., Rudie, G. C., et al. 2024, ApJL, 964, L12
Rynkun, P., Gaigalas, G., & Jönsson, P. 2019, A&A, 623, A155
Saintonge, A., Lutz, D., Genzel, R., et al. 2013, ApJ, 778, 2
Sanders, R. L., Shapley, A. E., Clarke, L., et al. 2023, ApJ, 943, 75
Sanders, R. L., Shapley, A. E., Reddy, N. A., et al. 2020, MNRAS, 491, 1427
Sanders, R. L., Shapley, A. E., Topping, M. W., Reddy, N. A., & Brammer, G. B. 2024, ApJ, 962, 24
Schaerer, D., Marques-Chaves, R., Barrufet, L., et al. 2022, A&A, 665, L4
Sharon, K., Bayliss, M. B., Dahle, H., et al. 2020, ApJS, 247, 12
Sharon, K., Cerny, C., Rigby, J. R., et al. 2022, arXiv:2207.05709
Stasińska, G. 2005, A&A, 434, 507
Storey, P. J., Sochi, T., & Badnell, N. R. 2014, MNRAS, 441, 3028
Storey, P. J., & Zeippen, C. J. 2000, MNRAS, 312, 813
Strom, A. L., Rudie, G. C., Trainor, R. F., et al. 2023, ApJL, 958, 11
Taylor, A. J., Barger, A. J., & Cowie, L. L. 2022, ApJL, 939, L3
Trump, J. R., Arrabal Haro, P., Simons, R. C., et al. 2023, ApJ, 945, 35
Trussler, J. A. A., Adams, N. J., Conselice, C. J., et al. 2023, MNRAS, 523, 3423
Virtanen, P., Gommers, R., Oliphant, T. E., et al. 2020, NatMe, 17, 261
Wuyts, E., Rigby, J. R., Gladders, M. D., et al. 2012, ApJ, 745, 86